JGR Earth Surface

RESEARCH ARTICLE
10.1029/2023JF007305

Coevolution of Rock Slope Instability Damage and Resonance Frequencies From Distinct-Element Modeling

E. K. Jensen[1] **and J. R. Moore**[1]

[1]Department of Geology and Geophysics, University of Utah, Salt Lake City, UT, USA

Key Points:

- Distinct-element modeling of progressive rock slope failures revealed resonance frequency decreases between 20% and 60%
- Frequency changes were correlated with open joint length and decreased most for failures dominated by steeply dipping fractures
- Distinct amplification patterns were observed across the landslide surface for varying failure mechanisms during progressive failure

Supporting Information:

Supporting Information may be found in the online version of this article.

Correspondence to:

E. K. Jensen,
erin.k.jensen@utah.edu

Citation:

Jensen, E. K., & Moore, J. R. (2023). Coevolution of rock slope instability damage and resonance frequencies from distinct-element modeling. *Journal of Geophysical Research: Earth Surface*, *128*, e2023JF007305. https://doi.org/10.1029/2023JF007305

Received 20 JUN 2023
Accepted 30 OCT 2023

Author Contributions:

Conceptualization: E. K. Jensen, J. R. Moore
Data curation: E. K. Jensen, J. R. Moore
Formal analysis: E. K. Jensen, J. R. Moore
Funding acquisition: J. R. Moore
Investigation: E. K. Jensen, J. R. Moore
Methodology: E. K. Jensen, J. R. Moore
Resources: E. K. Jensen, J. R. Moore
Supervision: J. R. Moore
Visualization: E. K. Jensen
Writing – original draft: E. K. Jensen
Writing – review & editing: J. R. Moore

Abstract Ambient vibration measurements can detect resonance frequency changes related to rock slope instability damage or boundary condition changes during progressive failure. However, the impact of slope kinematics on resonance changes and the expected form and sensitivity of frequency evolution during destabilization require clarification to improve the implementation of this technique across diverse settings. Since instrumented rock slope failures are rare, numerical modeling is needed to study the anticipated spectral response from in situ monitoring. We used 2D distinct-element modeling to evaluate the sensitivity and evolution of rock slope resonance behavior for slab toppling, flexural toppling, and planar sliding instabilities during progressive failure. Model simulations revealed that fundamental resonance frequency decreases between 20% and 60% with changes correlated with increasing length of open joints. Changes to higher-order frequencies associated with landslide sub-volumes were also detectable for cases with multiple fracture networks. Resonance behavior was most pronounced for failures dominated by steeply dipping open tension cracks, that is, flexural and slab toppling. Additionally, amplification patterns across the slope varied for the flexural toppling and sliding cases, providing potential new information with which to characterize landslide failure mechanisms using ambient vibration array measurements. Our results demonstrate landslide characteristics well-suited for in situ ambient resonance monitoring and provide new data describing the anticipated changes in resonance frequencies during progressive rock slope failure.

Plain Language Summary Monitoring the natural vibrations (or resonance frequencies) of unstable rock slopes using seismic instruments can indicate changes associated with possible collapse. However, the relationships between resonance frequency changes and rock slope stability are not well understood and need to be investigated to support future field applications. Since slope collapses are difficult to measure in situ, we used numerical rock mechanics modeling to study the behavior of different failure types. Our results showed that resonance frequency changes are strongly related to the presence and development of open cracks and generally decrease as rock slope failure progresses, although complex fracture patterns can cause variable frequency responses. Our results provide new information on the type of slope instabilities that can be best monitored using resonance frequency measurements, and the form of changes that can be anticipated from future field studies.

1. Introduction

In situ ambient vibration measurements can reveal resonance changes to unstable rock masses and are becoming increasingly utilized in slope stability monitoring (e.g., Bottelin, Jongmans, et al., 2013; Burjánek et al., 2010; Colombero et al., 2021; Häusler et al., 2019; Kleinbrod et al., 2019; Lévy et al., 2010). In rock slope instabilities, resonance originates from standing waves in a compartment decoupled along one or more fractures, or material stiffness contrasts between fractured zones and the adjacent intact rock mass (Bottelin, Jongmans, et al., 2013; Burjánek et al., 2018, 2019; Kleinbrod et al., 2019). The dependency of a rock slope's resonance frequencies on mass and stiffness (Chopra, 2012) implies that internal or boundary condition changes affecting one or both properties are detectable through continuous or repeated frequency measurements. Demonstrated decreases in resonance frequencies before the failure of a rock column (Lévy et al., 2010) and a rock block collapse test (Taruselli et al., 2020), in addition to results of a study showing an increase in resonance frequencies of an unstable rock compartment after bolting reinforcement (Bottelin et al., 2017), highlight ambient vibration measurements as a valuable slope stability monitoring technique. Although numerous additional field-based studies have attempted to capture frequency changes associated with landslide destabilization, often only environmentally driven recoverable changes are recorded (Bottelin, Lévy, et al., 2013; Burjánek et al., 2018; Colombero et al., 2018, 2021; Dietze et al., 2021; Guillemot et al., 2022; Häusler et al., 2021, 2022; Weber et al., 2018). In addition to resonance frequency values, seismic parameters including frequency-dependent polarization azimuth and damping (e.g., Geimer et al., 2022) can be used to detect internal structural or material changes during stability monitoring (e.g., Häusler et al., 2022).

Although the resonance frequencies of a landslide are expected to decrease during progressive failure, scarce field data limits our understanding of the expected form and sensitivity of anticipated changes. Theoretical relations for the resonance frequencies of a cantilever beam have been used to analyze the behavior of unstable rock compartments and relate frequency changes to crack depth, geometry, and material stiffness (Bottelin, Jongmans, et al., 2013; Got et al., 2010; Iannucci et al., 2018; Valentin et al., 2017; Weber et al., 2018). However, such relations are not necessarily applicable to more complex landslide geometries, and the impact of slope failure kinematics on frequency changes has not been thoroughly studied. Field investigations have revealed resonance changes across different landslide compartments or zones due to material characteristics, geometry, and fracture patterns (Del Gaudio et al., 2013; Galea et al., 2014; Iannucci et al., 2018; Kleinbrod et al., 2019), providing indications of resonance changes expected with instability evolution. For example, strong spectral amplification and directivity are frequently observed in the presence of steeply dipping open cracks, reflecting normal mode vibration of the main landslide body at a fundamental (or first resonance; f_1) frequency and vibration of secondary volumes or sub-blocks at higher frequencies (Burjánek et al., 2010, 2012, 2018; Häusler et al., 2019, 2022; Moore et al., 2011).

Since appropriately instrumented rock slope failures occur infrequently, numerical modeling represents a valuable complement to field experiments investigating progressive failure. Distinct element methods are commonly used to model jointed rock masses (Cundall, 1980; Cundall & Hart, 1992), including landslides in rock (Eberhardt et al., 2004; Fischer et al., 2010; Gischig et al., 2011a, 2011b; Grämiger et al., 2017; Lorig et al., 2009; Mamot et al., 2021). In particular, recent studies have employed numerical modeling to reproduce the observed amplification characteristics and resonance behavior of unstable rock sites using dynamic wave propagation (Burjánek et al., 2019; Glueer et al., 2021; Moore et al., 2011). Additionally, numerical experiments have demonstrated a decrease in the fundamental frequency of rock slopes with increasing depth and decreasing fracture stiffness (Burjánek et al., 2019; Gischig et al., 2015) and shown changes in amplification patterns across progressively damaged slopes during seismic fatigue (Gischig et al., 2016).

Here, we build on past field and numerical studies to evaluate the sensitivity and evolution of rock slope resonance properties for different kinematic failure modes. Given the anticipated seismic response of steeply dipping open fractures, we hypothesize that instability resonance properties will be most detectable for geometries with prevalent internal extension (e.g., toppling) and may have a less distinct resonance response for failures dominated by other modes, such as planar sliding. We used the Universal Distinct Element Code (UDEC; Itasca Consulting Group, 2019) to simulate progressive destabilization of different failure types and recovered the resonance behavior of increasingly damaged model states. Analysis of spectral properties in relation to displacements and joint fracture enabled assessment of landslide frequency evolution to identify failure scenarios that are well-suited for in situ ambient resonance monitoring and provide new information on the form and sensitivity of anticipated frequency responses. We compare model outputs with field analogs, including the Courthouse Mesa rock slope instability in Utah, USA, for which we have conducted field characterization and long-term monitoring (Bessette-Kirton et al., 2022).

2. Methods

2.1. Failure Scenarios and Modeling Approach

We conducted numerical modeling experiments using three types of rock slope instabilities to investigate the sensitivity and evolution of resonance properties during progressive failure. Our first evaluated kinematic failure mode was toppling of a single rock body (block, column, or slab) from the propagation of a rear bounding fracture (e.g., Wyllie, 1980), which we herein refer to as slab toppling (Figure 1a). Slab toppling failures are common in granitic rocks (e.g., Colombero et al., 2018), anaclinal slopes in hard limestone cliffs (Frayssines & Hantz, 2009) and interbedded sandstones and mudstones, where undercutting from differential weathering initiates toppling and the propagation of tension cracks at the crest of the slope (Wang et al., 2013). This case was chosen because it is common to many investigations of resonance in unstable rock compartments (Bottelin et al., 2017; Bottelin, Jongmans, et al., 2013; Bottelin, Lévy, et al., 2013; Colombero et al., 2018, 2021; Lévy

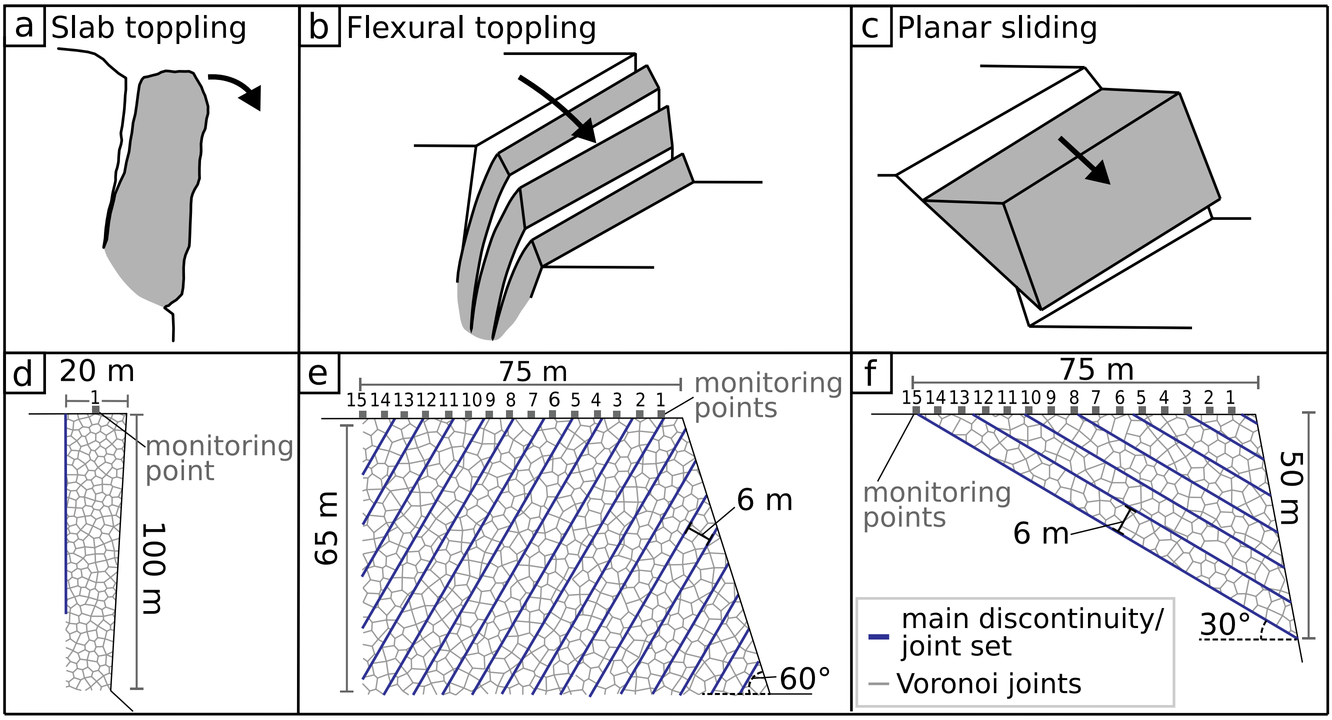

Figure 1. Examined rock slope failure types. Schematic diagrams and images showing the model setup for (a and d) slab toppling, (b and e) flexural toppling, and (c and f) planar sliding. Images of model setups (d)–(f) show the main discontinuity or joint set (blue), Voronoi joints (gray), and monitoring points (gray squares) for each model. Panels (b and c) are modified from Wyllie and Mah (2005).

et al., 2010) and reflects the geometry of our Courthouse Mesa field site, which was used for comparison with model results (Bessette-Kirton et al., 2022). We also examined two common kinematic failure modes: flexural toppling and planar sliding (Figures 1b and 1c). Flexural toppling occurs in slopes with a preferred discontinuity system of joints dipping steeply (>50°) into the slope and involves rock columns breaking in flexure during rotation (Goodman & Bray, 1976). Planar sliding involves the movement of one or multiple rock blocks along failed discontinuity surfaces that daylight on the slope face (Higgins & Andrew, 2012).

Discontinuum modeling is a numerical method representing the mechanical behavior of discontinuities and solid materials using an assemblage of discrete blocks intersected by joints. The distinct element method, as applied in UDEC, is a 2D discontinuum numerical approach that (a) uses an explicit time-marching solution to solve the equations of motion, (b) can include rigid or deformable blocks, and (c) uses finite normal joint stiffness (i.e., soft-contact assumption) (Cundall, 1980; Cundall & Hart, 1992; Itasca Consulting Group, 2019). An explicit time-marching solution scheme is advantageous for complex, non-linear problems because it accounts for the path needed to reach a solution (Itasca Consulting Group, 2019). Blocks are separated by discontinuities along which shear and tensile mode failures can occur, allowing for large displacements and block rotations. If blocks are set as deformable, they are discretized into finite difference zones, and a specified constitutive model governs deformation. Blocks are typically set as either elastic (in cases where failure is dominated by slip along discontinuities) or plastic (e.g., using a Mohr-Coulomb failure criterion). Joints are also assigned a constitutive model that governs failure and can be modeled with either linear or nonlinear behavior of varying complexity.

We utilized UDEC's static and dynamic modeling capabilities in a coupled approach where we simulated stages of progressive failure using static models and then used dynamic models to investigate the resonance characteristics of each failure state. In UDEC, static models solve a damped version of the equations of motion in which the damping force at each point is proportional to the unbalanced force at that location (Itasca Consulting Group, 2019). Static models are solved using a number of steps to reach equilibrium and therefore do not have a component of actual time. In contrast, dynamic models simulate the time-dependent response to a transient input. Dynamic models solve for the full equations of motion and utilize Rayleigh damping to simulate energy losses as approximately frequency-independent in a prescribed frequency range (Itasca Consulting Group, 2019).

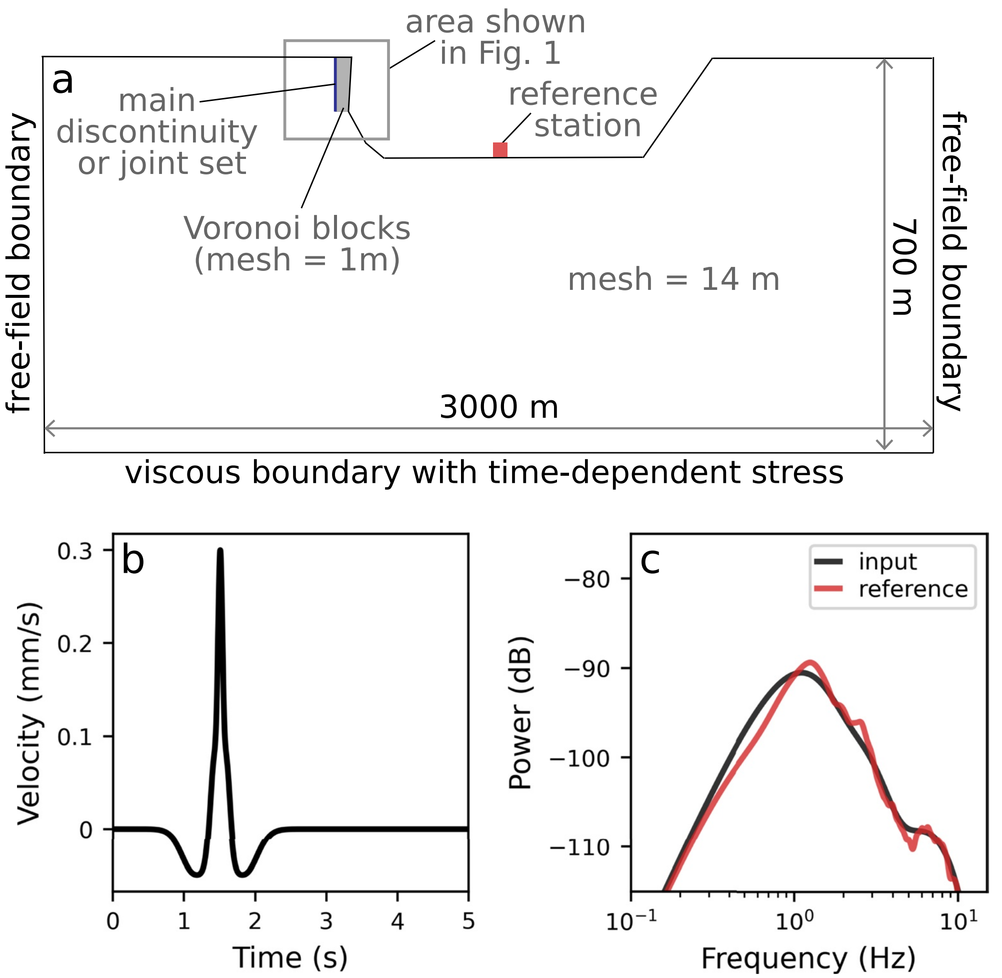

Figure 2. UDEC model setup. (a) Schematic diagram of the model half space showing boundary conditions used for dynamic modeling. (b) Velocity time series of the input Ricker wavelet (superposition of 1, 2, and 6 Hz wavelets) applied at the bottom model boundary for dynamic runs. (c) Power spectral density curves for the input Ricker wavelet (black) and recorded at the valley reference station during dynamic modeling (red; corresponds to the red square in part (a). Decibel powers are relative to 1 m^2 s^{-2} Hz^{-1}.

2.2. UDEC Modeling

2.2.1. Model Setup

For each kinematic case, we embedded the modeled rock slope instability in a 3,000 m wide x 700 m tall half space to minimize boundary effects during dynamic modeling (Figure 2a; Gischig et al., 2015). We constructed each geometry with an exposed cliff height between 50 and 100 m, with jointed areas of 1,750, 5,525, and 1,350 m^2 for the slab toppling, flexural toppling, and planar sliding cases, respectively. Although the total jointed area for the flexural toppling case is larger, only about half of the area experiences damage. These were selected to maintain an approximately similar failure area across all kinematic modes. Since the Courthouse Mesa field site, which is associated with the slab toppling case, consists of massive sandstone (Bessette-Kirton et al., 2022), we chose to use the properties of sandstone for all scenarios to maintain consistency across models. We kept the following material properties constant: density = 2,000 kg/m^3 (Moore, Geimer, Finnegan, & Thorne, 2018), Young's modulus = 10 GPa (based on data from Entrada, Navajo, and Wingate Sandstones in Utah; Alikarami et al., 2013; Moore, Geimer, Finnegan, & Thorne, 2018; Skurtveit et al., 2021), and Poisson's ratio = 0.2. For realistic wave propagation during dynamic modeling, the maximum mesh size should be 1/8 to 1/10 of the wavelength associated with the highest frequency wave propagating through the model (Itasca Consulting Inc., 2019). Based on the selected rock properties, we calculated seismic velocity as $V_S = 1{,}443$ m/s; thus, to allow for maximum frequencies between 10 and 13 Hz, we implemented a mesh size of 14 m. This value was assigned to the entirety of the

Table 1

Peak Joint Strength Properties Applied in Progressively Damaged Slab Toppling (s0–s7), Flexural Toppling (t0–t7), and Planar Sliding (p0–p6) Models

Kinematic mode	Run	c_{eq} (MPa)	ϕ_{eq} (°)
Slab toppling	s0	1.7	24
	s1	1.6	23.7
	s2	1.5	23.5
	s3	1.4	23.3
	s4	1.3	23.1
	s5	1.2	22.8
	s6	1.1	22.6
	s7	1.0	22.4
Flexural Toppling	t0	0.38	34.9
	t1	0.32	32
	t2	0.28	30
	t3	0.24	28
	t4	0.2	25.8
	t5	0.16	23.5
	t6	0.14	22.4
	t7	0.1	20
Planar Sliding	p0	0.4	21.0
	p1	0.38	20.9
	p2	0.35	20.85
	p3	0.33	20.8
	p4	0.25	20.6
	p5	0.15	20.35
	p6	0.05	20.1

half space, except for the instability area, where we assigned a mesh size of 1 m. All blocks were modeled with isotropic elastic properties.

For each failure scenario, we constructed a joint set (flexural toppling and planar sliding) or single rear discontinuity (slab toppling) and used a randomized Voronoi tessellation generator (Itasca Consulting Group, 2019) to split the instability into blocks with a maximum edge size of 3 m (e.g., Gischig et al., 2015, 2016). Thus, each scenario consisted of a main discontinuity or joint set and a joint set bounding the Voronoi blocks. We applied a Coulomb slip constitutive model with residual strength to all joints (Itasca Consulting Group, 2019). For the flexural toppling and sliding models, failure was controlled by the strength properties of the main joint set, and we kept the strength properties of the Voronoi joints constant to simulate the failure of intact rock. In the case of the Courthouse Mesa instability the rear discontinuity did not initiate along a predefined joint surface (e.g., Bessette-Kirton et al., 2022). Therefore, for the slab toppling model, we applied the same properties to the main discontinuity and Voronoi joints, since the rupture of the main discontinuity involves fracture of intact rock rather than predefined joint surfaces.

2.2.2. Model Initialization

To initialize stresses in the model half space, we ran several steps to arrive at the model geometry prior to simulating rock slope failure. First, we constructed a rectangular half space and applied high strength values (angle of friction (ϕ) = 60°, cohesion (c) = 100 MPa, and tension (T) = 100 MPa) to all joints. These values were chosen to prevent failure during the initialization phase. We then applied boundary conditions and initialized gravitational stresses in the rectangular block model. A stress gradient was applied to lateral boundaries for consistency with initialized in situ stresses, and a fixed velocity boundary condition was applied at the base of the model. In a second step, to ensure realistic initialization of topographic stresses, we excavated the model half space to create a valley with the instability area situated on the valley flank (Figure 2a). With high joint strength values still applied, we solved for equilibrium under gravitational loading. This initial stress state was the starting point for subsequent damage state models.

2.2.3. Static Damage State Models

We simulated progressive failure by incrementally reducing peak joint strength properties and solving for mechanical equilibrium under gravitational stress. To gradually reduce strength properties, we used an empirical approach (Jennings, 1970) that represents discontinuity strength properties based on a specified proportion of rock bridges:

$$c_{\mathrm{eq}} = (\%\mathrm{RB})c_i + (1 - \%\mathrm{RB})c_j \tag{1}$$

$$\tan\phi_{\mathrm{eq}} = (\%\mathrm{RB})\tan\phi_i + (1 - \%\mathrm{RB})\tan\phi_j \tag{2}$$

This technique uses a combination of strength values for intact rock (cohesion, c_i and friction angle, ϕ_i) and joints (c_j and ϕ_j) to formulate values of equivalent cohesion (c_{eq}) and friction angle (ϕ_{eq}) as a function of rock bridge percentage (%RB). The approach allows for an empirically based, stepwise adjustment of joint strength properties by reducing %RB. We used strength properties of sandstone from previous experimental studies and followed procedures outlined in past numerical modeling studies to obtain intact rock and joint strength properties. Peak and residual strength properties were obtained from Barton (1976), Barton and Choubey (1977), Goodman (1989), Kulhawy (1975), and Wyllie and Norrish (1996). These values were used in Equations 1 and 2 to formulate equivalent strength properties (c_{eq} and ϕ_{eq}) as a function of %RB (e.g., Gischig et al., 2011b). Since tensile strength is not derived directly from Equations 1 and 2, we calculated equivalent tension (T_{eq}) as $c_{\mathrm{eq}}/10$ following Eberhardt et al. (2004) and Gischig et al. (2015). For static models, c_{eq}, T_{eq}, and ϕ_{eq} were prescribed in UDEC as peak joint strength properties (Table 1), whereas residual joint strength, and stiffnesses (peak and residual) were held constant

Table 2
Peak and Residual Joint Strength and Stiffness Properties Applied in UDEC Models

	All joints							Voronoi joints		
Kinematic mode	c_r (MPa)	T_r (MPa)	ϕ_r (°)	k_n (GPa/m)	k_s (GPa/m)	k_{nr} (GPa/m)	k_{sr} (GPa/m)	c_{pv} (MPa)	T_{pv} (MPa)	ϕ_{pv} (°)
Slab Toppling	0	0	20	10	5	1	0.5	See values in Table 1		
Flexural Toppling	0.1	0	20	10	5	1	0.5	5	0.1	40
Planar Sliding	0	0	20	10	5	1	0.5	0.8	0.08	21.9

Note. Values of residual cohesion (c_r), residual tensile strength (T_r), residual friction angle (ϕ_r), and peak and residual normal and shear stiffness (k_n, k_s, k_{nr}, k_{sr}) were held constant for all joints in each failure scenario. Values of peak Voronoi cohesion (c_{pv}), peak Voronoi tension (T_{pv}), and peak Voronoi friction angle (ϕ_{pv}) were also held constant for the flexural toppling and planar sliding models.

(Table 2). Peak shear and normal stiffness values were obtained from Gischig et al. (2015), Fischer et al. (2010), and Eberhardt et al. (2004). We performed several simple sensitivity tests to assess and assign values for residual stiffness. After applying joint properties, we solved for static equilibrium and assessed the damage state of each model by recording the length of open (defined as normal force = 0) and failed joints as well as horizontal displacements.

2.2.4. Dynamic Rock Slope Models

Since we aimed to only simulate fracture propagation during static modeling and subsequently used dynamic modeling to measure ambient vibrations for each damage state, we applied high strength properties (as in Section 2.2.2) to all joints to prevent additional damage during this step. We also applied shear and normal residual stiffness values of 0.5 GPa/m and 1 GPa/m, respectively, to all failed joints (Table 2). To reduce wave reflections at the model boundaries, we applied an absorbing viscous boundary at the bottom of the model and free-field boundaries, which simulate an infinite continuum, to the sides (Itasca Consulting Group, 2019). We then assigned a superposition of Ricker wavelets as a dynamic input at the base of the model (Asimaki & Mohammadi, 2018; Gischig et al., 2015; Glueer et al., 2021; Figure 2b). We chose the superposition of 1, 2, and 6 Hz wavelets since this combination most evenly excited frequencies between 0.5 and 10 Hz (Figures 2b and 2c). Implementation of a viscous bottom boundary necessitated the use of a stress input. Accordingly, we converted the Ricker wavelet velocity history to a shear stress history following Equation 3 and applied the horizontal stress component (σ_s) as a function of time (t) at the base of the model.

$$\sigma_s(t) = 2\rho V_S v_s(t) \tag{3}$$

Here σ_s is shear stress, ρ is material density, V_s is s-wave velocity, and v_s is the horizontal input velocity. We implemented Rayleigh damping using a damping factor of 0.1% and center frequencies of 2 Hz for the slab toppling model and 4 Hz for the flexural toppling and sliding models. Center frequencies were selected based on a desired output frequency range of 0.1–10 Hz (Itasca Consulting Group, 2019) and the anticipated resonance frequencies for each case. We generally expected a lower resonance frequency for the slab toppling case since the instability is bounded by a vertical rear fracture. Conversely, we anticipated more internal fracturing and the formation of smaller-volume blocks (with higher resonance frequencies) for the flexural toppling and planar sliding cases.

Dynamic models were run for 20–35 model seconds (run times ranged between 10 and 50 hr) to achieve a desired frequency resolution of ~0.05 Hz. We recorded velocity time series at several monitoring points on each slope instability (Figures 1d–1f) and at additional reference points distributed throughout the model (e.g., Figure 2a). For the slab toppling case, we used a single monitoring point centered on the slab, whereas for the sliding and toppling cases, we used 15 monitoring points with 5-m-spacing distributed across the top surface of the landslide. UDEC time-series outputs are available in Jensen and Moore (2023).

2.3. Spectral Analysis

We post-processed time-series outputs from UDEC to analyze resonance behavior in the frequency domain. All processing was performed using the NumPy Python package (Harris et al., 2020). We converted velocity time-series data to the frequency domain using the discrete fast Fourier Transform (FFT). Prior to calculating the FFT, we applied a Hanning taper to reduce spectral leakage. From the FFT, we calculated power spectral densities and spectral amplitude ratios to track peaks corresponding to resonance frequencies of the instability (e.g., Burjánek et al., 2018; Finnegan et al., 2022; Kleinbrod et al., 2019). The spectral response of the valley

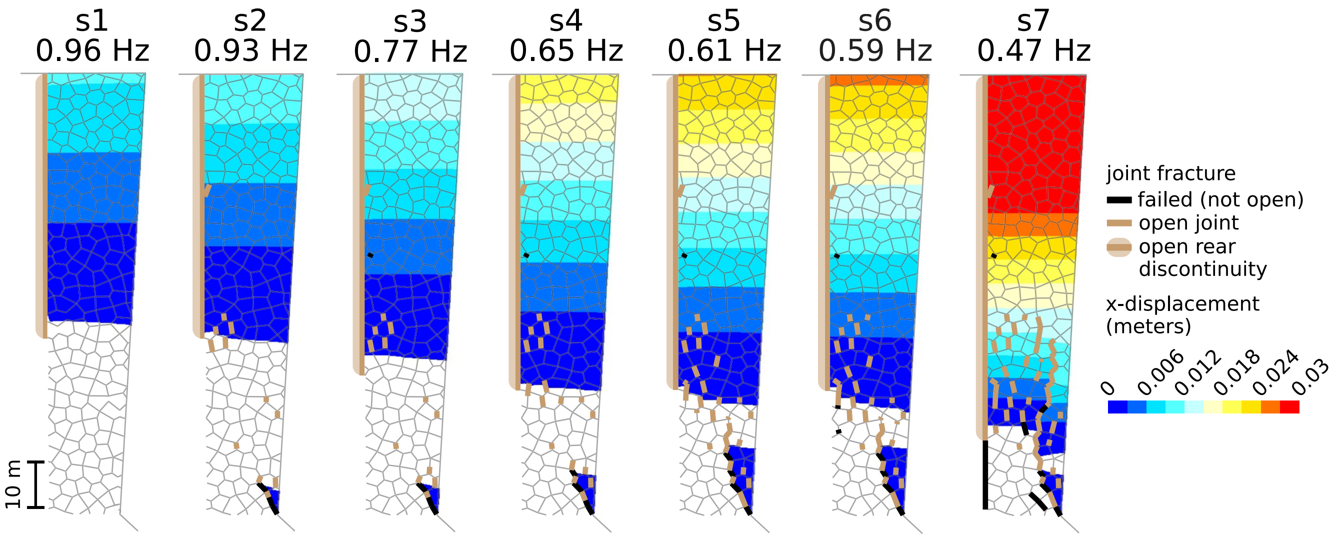

Figure 3. Horizontal displacement fields and fracture patterns for progressively damaged slab toppling models s1–s7. The open length of the rear discontinuity is shown with a thick brown line, whereas internal joint fracture is shown with thin black (failed) and brown (open) lines.

floor reference station closely matched that of the Ricker Wavelet (Figure 2c); therefore, for clarity, we calculated amplitude ratios with respect to the input wave. Minor differences in the spectra of the input wave and the response recorded at the valley reference station indicate the presence of surface effects; however, these are minimized at this station since it is located relatively far from the cliff edge. Since our models use an input motion with a set frequency range and corresponding amplitude variations, the amplitude of model outputs is partially influenced by the input wave, complicating comparisons of spectral amplitudes across model stages. We thus primarily use amplitude ratios to examine the relative response across the slope during progressive model stages.

3. Results

3.1. Slab Toppling

Slab toppling failure was dominated by progressive downward propagation and opening of the rear slab-bounding discontinuity. Additionally, internal failure of Voronoi joints due to compressional stresses resulting from the overhanging geometry of the slab originated at the toe of the slab and propagated upward (Figure 3). Displacement was normal to the main crack and maximum at the top of the slab. We simulated resonance for the unfailed model (labeled s0) and seven progressively damaged models, s1–s7 (Table 1). Resonance of the column in the evaluated frequency range was expressed as a single spectral peak with amplification over a narrow frequency band. Overall, the frequency decreased with increased fracture and opening of the main discontinuity (Figures 4a and 4b). The progressive narrowing of spectral peaks during subsequent failure stages also indicates a reduction in damping. As described in Section 2.3, the amplitudes of these peaks are partially influenced by the amplitude of the input motion; therefore, we do not further interpret amplitude changes between failure stages. The resonance frequency of the column emerged at 0.96 Hz with initial failure and opening of the rear fracture to a depth of 56 m (s1). Subsequently, the frequency decreased to 0.77 Hz (s3) and ~0.6 Hz (s4–s6) with crack propagation and opening to depths of 63 and 67 m, respectively. During the final failure stage (s7), the rear discontinuity failed to a depth of 92 m with an open depth of 78 m, resulting in a resonance frequency of 0.47 Hz (Figures 4a and 4b). Between stages s1 and s7, frequency decreased by 51% (~0.5 Hz). Initially, internal failure was minimal, with <5% of Voronoi joints open and/or fractured during stages s1–s4. During the final stage (s7), 12% of Voronoi joints were fractured, and 9% of Voronoi joints were open (Figure 3). Crack-normal displacement increased gradually during early failure stages before nearly doubling, with a maximum of 46 mm at the top of the column during the final stage (Figure 4c).

3.2. Flexural Toppling

Flexural toppling failure initiated through shear and tensile fracture of the main joint set with the development of open tension cracks near the slope crest. We assessed seven damage states of flexural toppling failure (t1–t7) and compared resonance simulations with the unfailed model, t0 (Table 1). Upon initial failure (t1), a broad peak

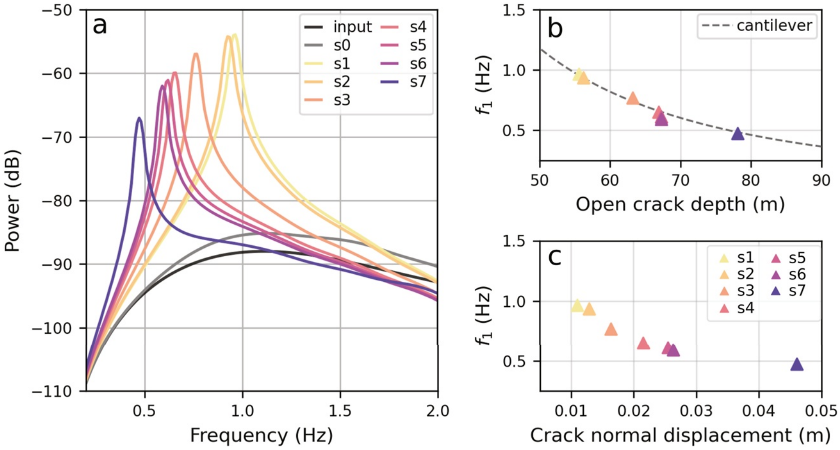

Figure 4. Slab toppling model results. (a) Power spectral density curves for damage states s1–s7 (colored lines) showing spectral peaks associated with the fundamental resonance frequency of the slab. The spectrum for the unfailed model (s0) is shown in gray, and that of the input Ricker wavelet is shown in black. Decibel powers are relative to 1 $m^2 s^{-2} Hz^{-1}$. (b) Fundamental frequency (f_1) plotted against open crack depth of the main rear discontinuity for progressive damage states in comparison to an analytical curve for a cantilever beam (see Section 4.1.1). (c) Fundamental frequency (f_1) plotted against crack-normal displacement at each stage.

emerged on station M1 at 3.3 Hz (Figure 5a). For clarity, we only show spectra from M1 (up to 5 Hz); spectra for all stations (up to 10 Hz) are included in Figure S1 of Supporting Information S1. Amplitude ratios show that this peak was consistent across the front 45 m of the slope (stations M1–M10; Figure 6a). See Figure S3 in Supporting Information S1 for all amplitude ratio data. Amplifications were highest at the back of the area delineated by fractures (station M10). Failure progressed through shear and tensile fracture of toppling joints and increasing internal failure. During stages t2 and t3, the peak at station M1 decreased and was amplified in a narrower frequency range, with peaks at 2.7 and 2.1 Hz (Figure 5a). During stage t2, this peak also appeared on stations M2–M10, but during stage t3, the peak was only visible across stations M2–M6, with amplification at 2.5, 4.2, and 1.9 Hz on stations M7, M8–M9, and M10, respectively (Figures 6b and 6c). In subsequent stages, the peak at M1 decreased to 1.6 Hz (stages t4–t6) and 1.3 Hz (stage t7; Figure 5a) and was shared across stations M1–M5 (Figures 6d–6f). In addition to the downward extension of the main joint set and increasing internal fracture, failure propagated backward during stage t5, extending to all but the rear 15 m of the slope. Amplification on stations M11–M12 (4.1 Hz) and M13 (5.8–6.6 Hz) appeared with the backward propagation of failure. Additionally, amplification

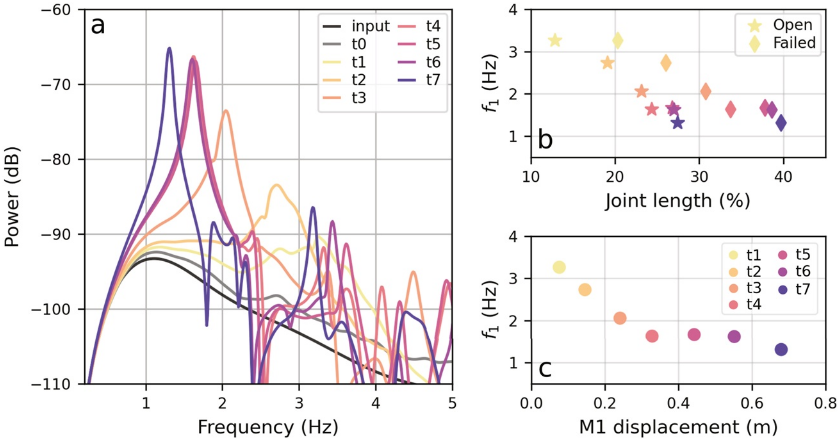

Figure 5. Flexural toppling model results. (a) Power spectral density curves for damage states t1–p7 (colored lines) at the slope crest (station M1) showing spectral peaks associated with the fundamental frequency of the instability. The spectrum for the unfailed model (s0) is shown in gray, and that of the input Ricker wavelet is shown in black. Decibel powers are relative to 1 $m^2 s^{-2} Hz^{-1}$. See Figure S1 in Supporting Information S1 for frequencies up to 10 Hz. b) Fundamental frequency (f_1) at M1 plotted against the percentage of failed (diamonds) and open (stars) joints for progressive damage stages. Colors correspond to the legend in part (c). (c) Fundamental frequency (f_1) at M1 plotted against displacement at the same location.

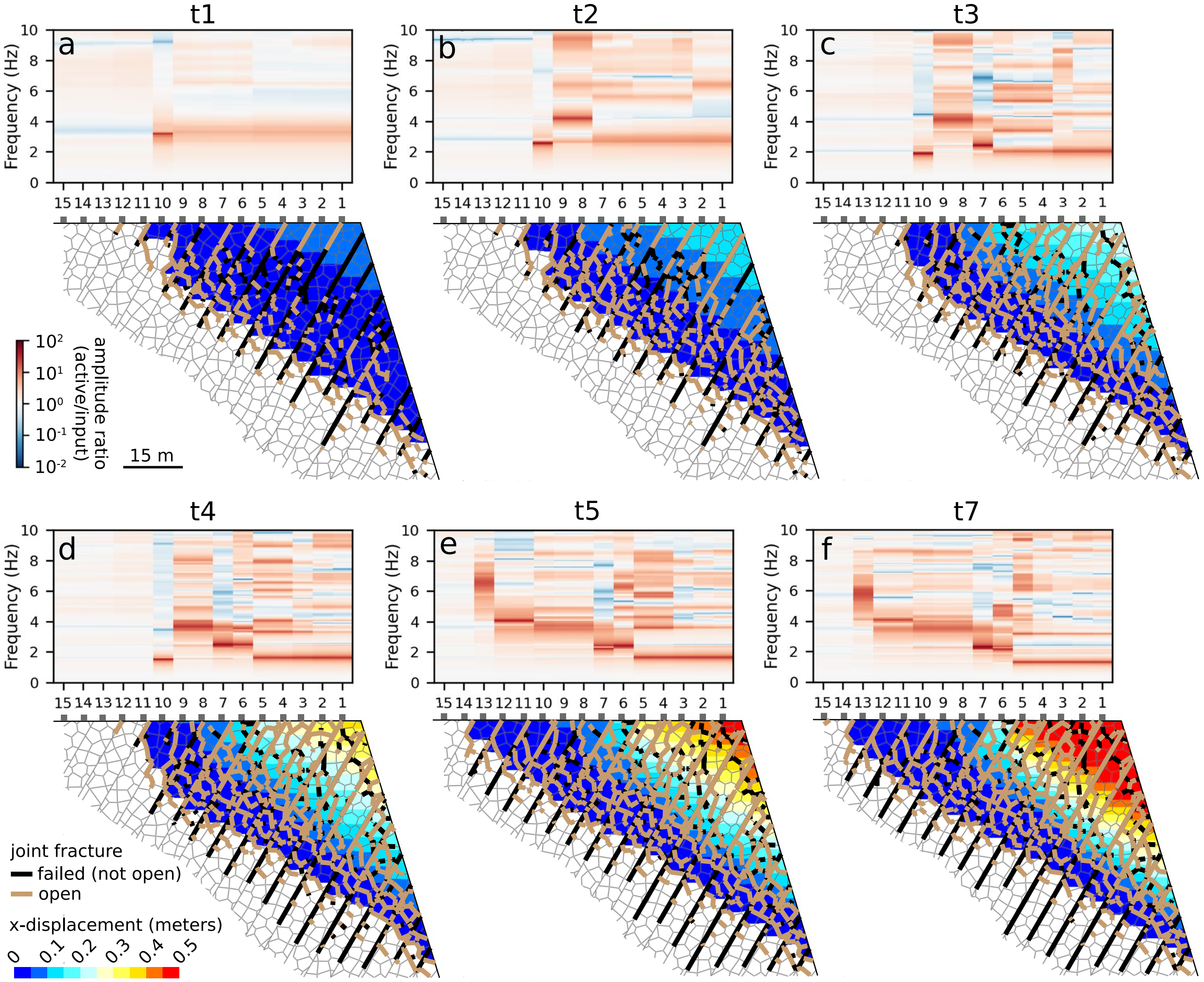

Figure 6. Horizontal displacement fields and amplitude ratio heat maps for progressively damaged flexural toppling models (a) t1, (b) t2, (c) t3, (d) t4, (e) t5, and (f) t7. The amplitude ratio values for monitoring stations 1–15 (gray squares) align with their slope positions. Amplitude ratios are computed with respect to the input Ricker wavelet (Figures 2b and 2c). See Figure S3 in Supporting Information S1 for amplitude ratio data.

patterns showed the appearance and evolution of blocks in the middle of the slope near stations M6–M10 during the final stages of failure (Figures 6d–6f). The amplitude ratio response and fracture pattern for failure stage t6 were similar to that of t5 and for simplicity are not displayed in Figure 6.

The fundamental frequency of the main landslide body (measured at M1) evolved linearly with open joint length (Figure 5b). Between stages t1 and t7, the fundamental frequency at M1 decreased by 60% (~2.0 Hz). The percentage of total open joint length (main joint set and Voronoi joints) ranged from 13% (stage t1) to 27% (stage t7). During early failure stages, frequency also decreased linearly with the length of failed joints (Figure 5b). In contrast, during failure stages t5 and t6, frequency did not decrease with increases in both failed joint length (Figure 5b) and displacement (Figure 5c). During all failure stages, displacement was concentrated in the front 25–30 m of the slope and ranged from 80 to 700 mm at station M1.

3.3. Planar Sliding

We examined six planar sliding damage states (p1–p6) and compared resonance properties with the unfailed model p0 (Table 1). Planar sliding failure initially occurred via shear fracture along the basal joint plane, followed by the development of tensile fractures near the back of the slope (stage p1). Under these conditions, only subtle spectral

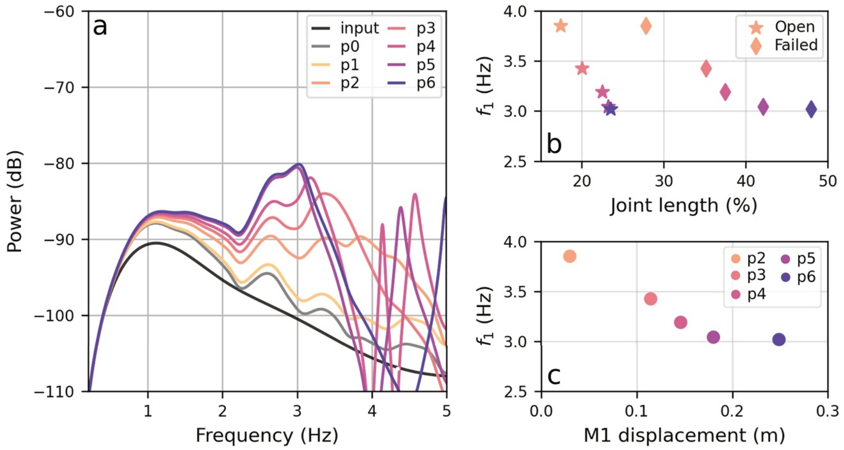

Figure 7. Planar sliding model results. (a) Power spectral density curves for damage states p1–p6 (colored lines) at the slope crest (station M1). Spectral peaks showing the fundamental frequency of the instability are visible for stages p2–p6. The spectrum for the unfailed model (s0) is shown in gray, and that of the input Ricker wavelet is shown in black. Decibel powers are relative to 1 $m^2 s^{-2} Hz^{-1}$. See Figure S2 in Supporting Information S1 for frequencies up to 10 Hz. b) Fundamental frequency (f_1) at M1 plotted against the percentage of failed (diamonds) and open (stars) joints for progressive damage states. Colors correspond to the legend in part (c). (c) Fundamental frequency (f_1) at M1 plotted against displacement at the same location.

peaks were visible on monitoring station M1 (closest station to the crest of the slope; Figures 7a and 8a). Spectra for all other stations are shown in Figure S2 of Supporting Information S1. As shown in Figure 8, during successive stages, additional shear fractures propagated at the base of the landslide, and tension cracks opened in the middle and toward the crest of the slope. Amplitude ratios across the landslide surface showed that the resonance of the main landslide body became apparent during stage p2 when a broad peak emerged at 3.9 Hz on stations M1–M5 (Figures 7a and 8b). See Figure S4 in Supporting Information S1 for all amplitude ratio data. A second, higher peak just below 6 Hz was also visible on stations M1–M5. In stages p2–p4, displacement was concentrated along the front 25 m of the slope (stations M1–M5). Subsequently, the broad spectral peak narrowed and became stronger, decreasing to 3.4, 3.2, and 3.0 Hz during stages p3–p5, respectively (Figures 7a and 8c–8e). In contrast, the peak at 6 Hz became less distinct and inconsistent across stations M1–M5. As planar joints failed further back and upwards in the slope (stages p5 and p6), differential displacements of blocks within the landslide were controlled by the development of open fractures through the middle of the unstable body (Figures 8d–8f). In addition to spectral peaks at stations M1–M5, amplitude ratios across the array revealed amplification in different areas of the landslide body, corresponding most notably to spectral peaks at M9 and M10 (7–8 Hz; p1–p5) and at M6–M8 (7–9 Hz; p3–p5). During the final failure stage, p6, the peak at M1–M5 was unchanged (Figure 7a). Additional shear fractures ruptured within the front 25 m of the landslide, and the peaks at stations M9–M10 and M6–M8 merged at ~7.2 Hz.

During failure evolution, the fundamental frequency at station M1 decreased by 22% (~0.8 Hz) and varied linearly with the total length of open joints (main joint set and Voronoi joints). Between stages p2 and p6, relative open joint length increased from 17% to 24% (Figure 7b). The relationship between frequency and length of all failed joints followed a similar trend. Frequency also decreased linearly with displacement at station M1, except for stage p6, during which displacement increased but frequency remained constant (Figure 7c). Comparing the length of failed and open joints indicated that between stages p5 and p6, most of the new joint failure occurred in shear (i.e., joints did not open). Displacements at M1 (where values were close to maximum displacement at the crest of the slope) ranged from 8 mm in stage p1 to 250 mm during stage p6.

4. Discussion

4.1. Frequency Evolution During Progressive Failure

4.1.1. Instability Resonance

We observed decreasing fundamental resonance frequencies during progressive slope failure in all kinematic cases. Due to the relatively simple geometry of the slab toppling case, the resonance of the column was expressed

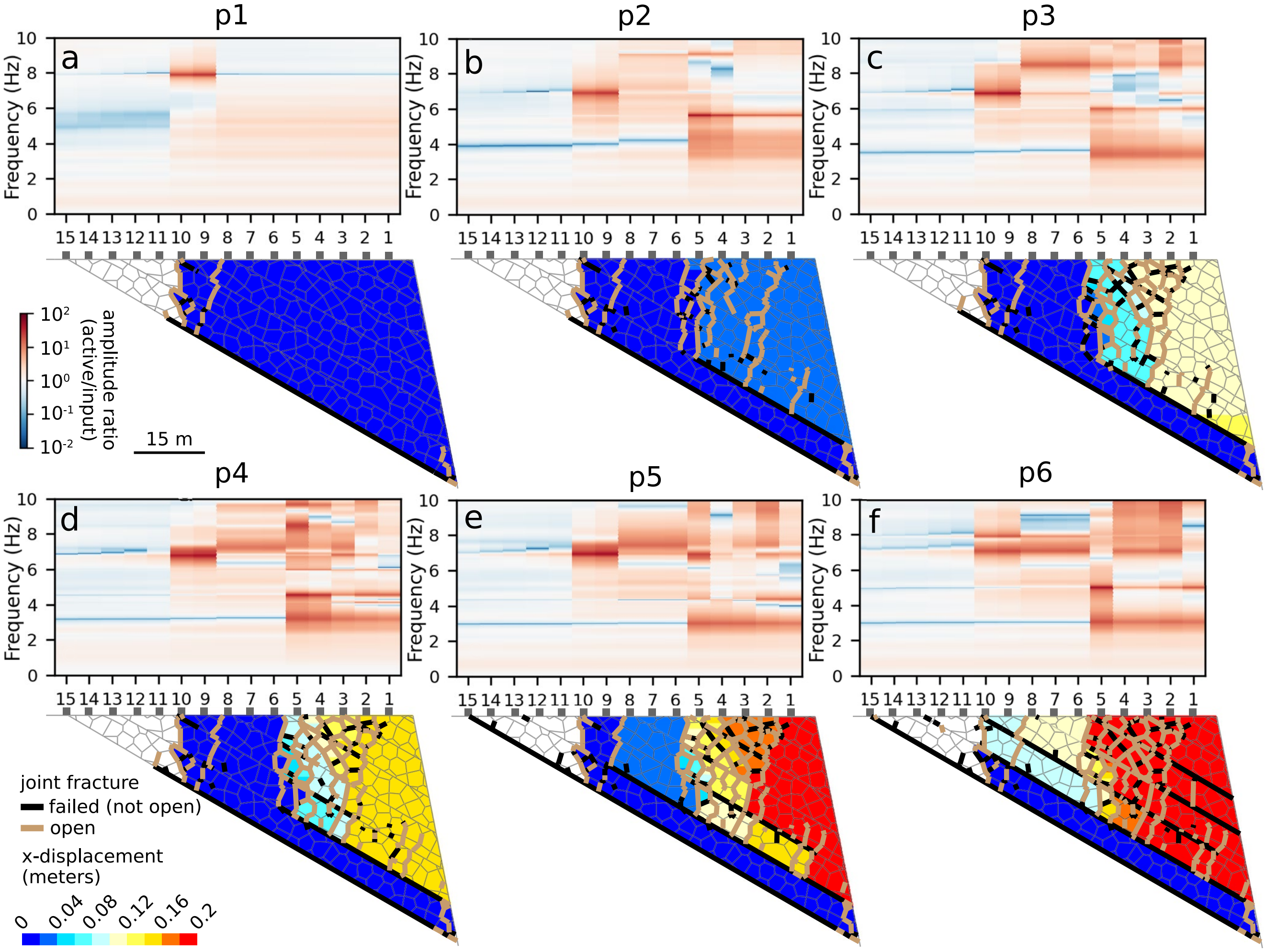

Figure 8. Horizontal displacement fields and amplitude ratio heat maps for progressively damaged planar sliding models (a) p1, (b) p2, (c) p3, (d) p4, (e) p5, and (d) p6. The amplitude ratio values for monitoring stations 1–15 (gray squares) align with their slope positions. Amplitude ratios are computed with respect to the input Ricker wavelet (Figures 2b and 2c). See Figure S4 in Supporting Information S1 for amplitude ratio data.

as a single spectral peak with amplification over a narrow frequency band, which was easily tracked during subsequent damage states. In contrast, adding joint sets introduced more complexity to the flexural toppling and sliding cases. For these geometries, global instability resonance could be reliably tracked at stations closest to the slope crest, whereas variable frequency responses corresponding to localized block development were observed in other areas of the slope. In the sliding case, spectral peaks at station M1 were broad and only subtly distinguishable from peaks at ~2.6 and ~3.4 Hz, which also appeared on spectra from the unfailed model (p0), and thus we attribute to topographic amplification of the cliff. During initial failure of the flexural toppling scenario, the spectral peak at M1 was also broad, but upon further damage accumulation, the peak narrowed and could be clearly tracked during progressive failure. For all failure cases, narrowing of the fundamental frequency peaks also demonstrates damping reductions accompanying progressive failure.

Frequency evolution for the slab toppling scenario generally followed the expected analytical expression relating resonance frequency (f) and length (L) of a cantilever beam:

$$f \sim L^{-2} \tag{4}$$

With increasing length, the resonance frequency of a cantilever decreases following a power law relationship. The geometry of the slab toppling model resembles a cantilevered column of increasing length (as depth of the open crack increases), and the resonance frequency is therefore anticipated to decrease approximately following Equation 4. Model results closely followed the expected trend for open crack depths of 55–80 m, corresponding to resonance frequencies between 1 and 0.5 Hz, respectively (Figure 4b). We also compared these results with a slab toppling model without internal failure (i.e., no Voronoi joints). Resonance frequencies similarly decreased with increasing open crack depth according to Equation 4. This indicates that increasing open crack depth controls frequency evolution for slab toppling failure, with only minor deviations from the analytical curve caused by internal fracturing and related heterogeneous material softening.

In contrast to the slab toppling case, resonance frequencies of the flexural toppling and sliding scenarios near the slope crest (as measured at station M1) decreased linearly with increasing length of open joints (Figures 5b and 7b). Our results showed that for both landslide geometries, resonance frequencies tracked more closely with the length of open joints than the length of all failed joints (i.e., combined tensile and shear failure). During some failure stages, we observed an increase in the length of failed joints with minimal changes in resonance frequency (e.g., stage p6 for sliding; stages t5 and t6 for toppling). This result demonstrates the importance of open cracks for the development of resonance behavior in unstable rock slopes. While additional joint fracture (in the absence of joint opening) could also lead to a reduction in stiffness, this impact may be muted for the complex failure patterns in the flexural toppling and planar sliding cases and is expected to be less dominant than the effect of fully open joints (e.g., Moore et al., 2012). For the flexural toppling and sliding scenarios, we observed no major differences in the frequency response to failure and opening of the repeating joint set compared to Voronoi joints.

We conducted simulations without Voronoi joints to further test the impact of internal failure on frequency changes for the flexural toppling and sliding cases. These tests only involved the failure of the controlling joint set. In the absence of internal fracturing, tensile failure of the toppling joint set resulted in the emergence of spectral peaks for blocks delineated by open cracks. However, these peaks were isolated, and there was no frequency response reflective of global instability damage (i.e., at the crest of the slope). In contrast, for the sliding model, the absence of internal failure resulted in shear fracture along 90% of the sliding joint set (with minimal open joints) and no change in the spectral response compared to the unfailed planar sliding model (p0). Thus, in contrast to the slab toppling case in which failure and opening of the main crack dominated frequency changes, internal failure was a critical control on the resonance response, enabling frequency tracking for more complex landslide geometries.

4.1.2. Flexural Toppling and Sliding Internal Block Evolution

For the flexural toppling and sliding cases, we observed spectral signals other than the peak corresponding to the resonance of the main landslide body in the evaluated frequency range (0.1–10 Hz). Comparisons of amplitude ratios across each array with displacement fields and fracture patterns (Figures 6 and 8) enabled the identification of distinct blocks within the landslide body and frequency changes uniquely associated with each failure stage. In Figures 9 and 10, we present interpretations of internal block development during progressive flexural toppling and sliding failures. We tracked resonance frequencies from stations on each landslide block to understand their frequency evolution, particularly when contrary to the consistent frequency decrease in the fundamental resonance mode.

During initial flexural toppling failure, the main landslide body (block A) was defined by open cracks near station M10 and a discontinuous shear plane from Voronoi joint failure at the base (see dashed lines in Figure 9a). The broad peak at 3.3 Hz on station M1 was common to stations M2–M10. The amplification of this peak was 6 times higher on station M10, indicating the presence of an internal subblock, B (Figure 9a). During stages t2 and t3, tensile failure near stations M7 and M8 delineated additional subblocks: block C with a resonance frequency of 4.2 Hz (stage t2, station M8; Figure 9b) and block D with a resonance frequency of 2.5 Hz (stage t3, station M7; Figure 9c). Block A was further subdivided during stage t4 with the development of an open crack between stations M5 and M6, forming block E (Figure 9d). The common spectral peak at 2.5 Hz on stations M6 and M7 showed that block E also encompassed block D. As previously shown, the fundamental resonance frequency measured at station M1 decreased consistently during subsequent failure stages (Figure 5). With the development of new blocks toward the back of block A, the resonance frequency of the main landslide body became visible across fewer array stations and was only visible on stations M1–M5 during later failure stages (t4–t7). During stage t5, tensile failure propagated further back in the slope, causing blocks B and C to combine and forming additional blocks F and G (Figure 9e). The spectral peaks on stations M8 and M10 converged at 3.7 Hz, and peaks appeared at 4.1 and 6.6 Hz on stations M11 and M13, respectively. Deeper failure of toppling joints and increased internal failure caused the frequencies of all blocks to decrease during stage t7 (Figure 9f).

Upon initiation of sliding failure, shear rupture at the base of the landslide and tensile failure near the back of the slope created a column delineated by open fractures and amplified at 7.9 Hz (block A; Figure 10a). Subsequently,

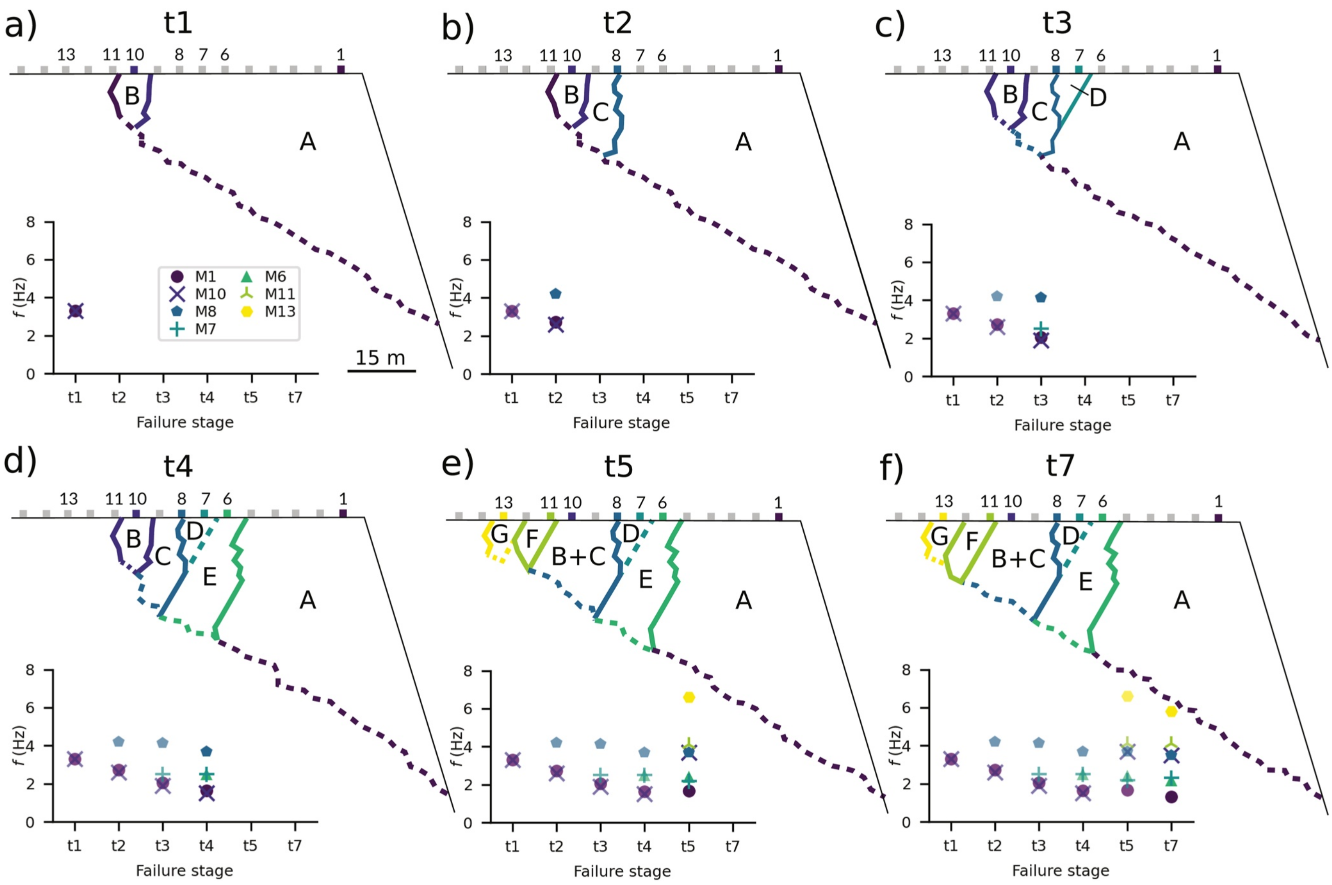

Figure 9. Schematic diagram showing block failure evolution and corresponding frequency changes for progressively damaged flexural toppling models: (a) t1, (b) t2, (c) t3, (d) t4, (e) t5, and (f) t7. Resonance frequency changes are shown in the insets for stations M1 (Figure 5a), M6, M7, M8, M10, M11, and M13 (Figure S1 in Supporting Information S1). Gray squares show the remaining monitoring stations. Dashed lines indicate discontinuous or uncertain failure planes.

shear failure along a second sliding joint near the crest of the slope and tensile failure between stations M5 and M6 created the main landslide block, B (Figure 10b). As discussed, the resonance frequency of block B decreased consistently during later model stages (Figure 7). During stage p2, a low-amplitude peak appeared at 9.1 Hz on stations M6–M8. We interpret this peak as the emergence of a third distinct block, C, able to resonate as a result of open cracks to the rear of station M8 and in front of station M6 (Figure 10b). A second-order peak on stations M1–M5 also appeared at 5.7 Hz and was amplified on stations M4 and M5 (block D; Figure 10b). In the following stages (p3 and p4), frequencies decreased for blocks A, B, and C (Figures 9c and 9d). After the frequency of block D decreased during stage p3, an additional peak appeared on station M5 at 8.5 Hz during stage p4, indicating an additional sub-block of D. The frequency for this peak decreased to 7 Hz during stage p5, and a peak common to stations M4 and M5 was no longer apparent. During stage p5, shear failure propagated at the base of block C, causing the peak on station M7 to increase in frequency slightly (Figure 10e). Finally, during stage p6, shear failure propagated toward the back of the slope, causing the joint at the base of blocks B and C to bisect block A. Stations M10 and M7 showed a spectral peak at 7.2 Hz, which was also apparent as a second-order peak on stations M2–M4, indicating the formation of a new block, E, encompassing blocks A, C, and part of B (Figure 10f). Station M10 also showed a second order peak at 8 Hz, interpreted as the resonance frequency of the remnants of block A embedded in block E.

4.1.3. Time-Dependent Frequency Response

Our stepwise modeling approach lacks a time component linking successive damage states. However, the crux of landslide monitoring involves time-to-failure predictions (Intrieri et al., 2019), such as the inverse-velocity approach (Fukuzono, 1985; Rose & Hungr, 2007) implemented using surface displacement or strain measurements (e.g., Crosta & Agliardi, 2003; Mufundirwa et al., 2010; Petley, 2004). To investigate the time-dependent

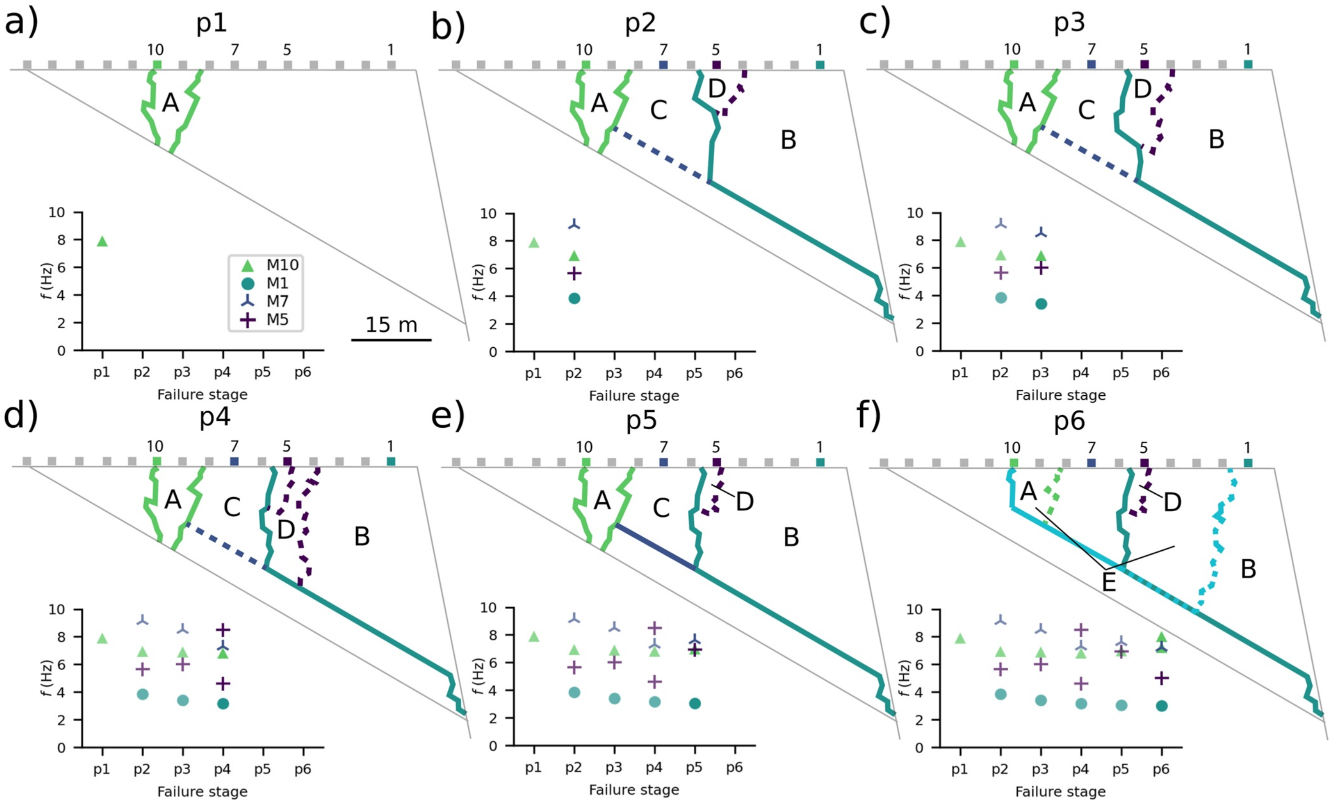

Figure 10. Schematic diagram showing failure evolution and corresponding frequency changes for progressively damaged planar sliding models: (a) p1, (b) p2, (c) p3, (d) p4, (e) p5, and (d) p6. Resonance frequency changes are shown in the insets for stations M1 (Figure 7a), M5, M7, and M10 (Figure S2 in Supporting Information S1). Gray squares show the remaining monitoring stations. Dashed lines indicate discontinuous or uncertain failure planes.

resonance response during progressive instability damage, we applied an inverse velocity framework to the results of our damage models. As commonly observed, we assumed that the terminal phase of failure is characterized by tertiary creep (Intrieri et al., 2019) and fits our modeled displacements (d) to the hyperbolic relation given in Equation 5 (Mufundirwa et al., 2010) to recover time (t) values for each damage state (Figure 11a).

$$d = -B\log(T_f - t) + C \tag{5}$$

We set the time-to-failure (T_f) as 30 days (arbitrary) and varied fitting parameters B and C to match modeled displacements for each kinematic case. Accordingly, the inverse of velocity for each scenario follows a linear trend with the time of failure occurring when inverse velocity = 0 (prescribed as 30 days; Figure 11a). In this analysis, the chosen value of 30 days as the time-to-failure does not impact the results since fitting parameters B and C are varied accordingly.

The resulting time-frequency relationships for each case show linear trends (Figures 11b and 11c). Slight deviations are apparent at the flexural toppling and sliding failure stages where frequency changes were minimal (i.e., p6, t5, and t6). During these stages, displacement increased, yet new damage occurred predominantly as failed but closed joints, minimizing changes in the frequency response. When normalizing by maximum frequency values, the linear trends for flexural and slab toppling cases show a similar slope (Figure 11c). A measured frequency decrease prior to natural rock slope failure has only been observed once with discontinuous data (Lévy et al., 2010), providing limited information on the anticipated form of frequency decrease during progressive damage. Since these previous data terminated ~2 weeks prior to ultimate slope collapse, it is difficult to compare with our models that capture the penultimate stages of failure. Our model results show that, regardless of failure type, if displacement follows a hyperbolic curve, frequency is expected to decrease linearly as time-to-failure approaches. Although this result requires the assumption that failure is in a tertiary creep phase and may not necessarily be valid in some scenarios, our analysis provides initial guidance on the previously unknown theoretical nature of frequency decreases accompanying slope failure. A step-failure time-displacement

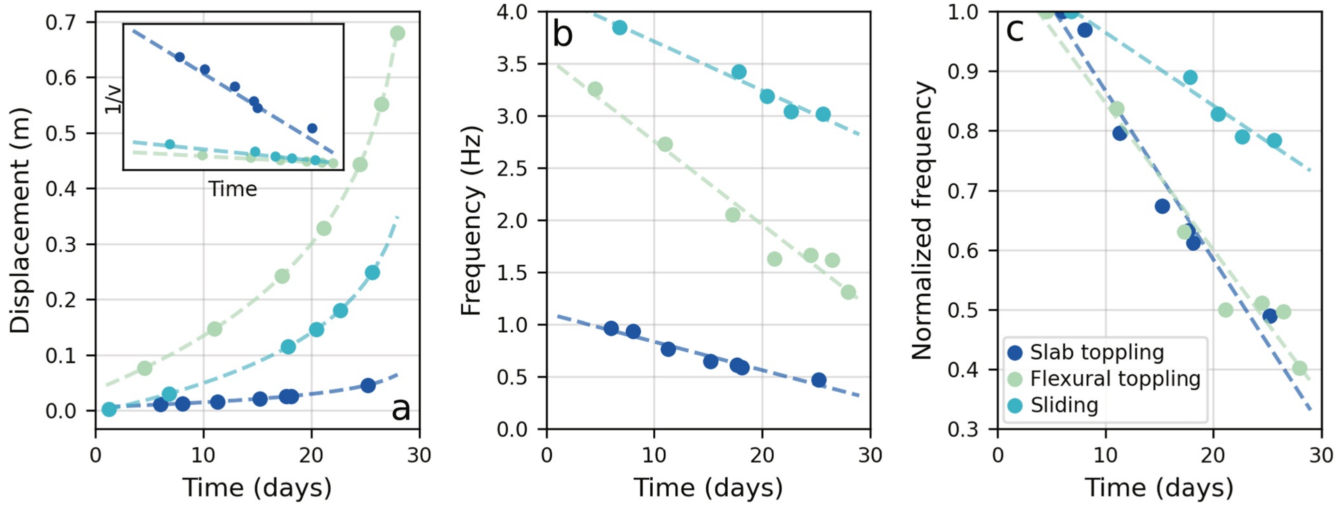

Figure 11. (a) Modeled displacements for the slab toppling (dark blue), flexural toppling (green), and sliding (light blue) scenarios plotted against hypothetical time values based on the prescribed fit to a hyperbolic curve. Inset axes show inverse velocity ($1/v$) versus time. (b) Raw and (c) normalized (by maximum frequency) resonance frequencies for each model stage plotted against hypothetical time values developed from the time-displacement curves shown in part (a). Resonance frequencies for the planar sliding and flexural toppling cases are from station M1.

relation could be more likely for the slab toppling case since new damage occurred primarily through failure and opening of the rear discontinuity, making this result potentially less valid for such geometries. In addition, unlike the observed hyperbolic increase in displacement preceding ultimate collapse, frequencies may not continually decrease beyond a certain damage state. For example, we observed increases in total joint failure and displacement with no accompanying frequency changes during the penultimate sliding and flexural toppling stages. Thus, frequency monitoring may be especially valuable for damage detection during early failure stages but may not be able to produce time-to-failure predictions like the inverse-velocity method in all final phases of progressive failure. Additional field data are needed to corroborate these results and further understand the time-evolution of frequency decreases during progressive failure.

4.2. Field Analogs and Implications for Slope Stability Monitoring

Model results showing a single, prominent spectral peak amplified over a narrow frequency range for the slab toppling case closely resemble field data collected at unstable rock columns and slabs (Bottelin, Jongmans, et al., 2013; Bottelin, Lévy, et al., 2013; Bottelin et al., 2017; Colombero et al., 2018, 2021; Lévy et al., 2010; Valentin et al., 2017). The clear decrease in frequency shown for progressively damaged slab toppling models indicates that ambient resonance monitoring is well-suited for this type of landslide geometry and would be expected to reveal clear frequency decreases with failure and opening of the rear discontinuity. Model results also showed that open crack depth dominated frequency changes, indicating that the resonance responses to internal damage (i.e., Voronoi joint failure) may be limited or undetectable. In contrast to our results, observations from a rock block collapse test showed that frequency decreases were also accompanied by the splitting of spectral peaks (Taruselli et al., 2020), suggesting that sites with small volumes or multiple joint sets may have more complex resonance evolution. In addition, higher modes could be more impacted by internal damage within the bulk instability since they are more sensitive to smaller volumes (Häusler et al., 2019).

Additional complexities in field monitoring data sets stem from frequency fluctuations related to meteorological effects (e.g., Colombero et al., 2021). For example, the frequency decrease measured before the collapse of an unstable rock column occurred during a period of temperature-driven frequency decrease punctuated by several rapid changes associated with precipitation events (Lévy et al., 2010). Meanwhile, the 50% frequency decrease recorded during progressive failure of our slab toppling model, which loosely mimics the Courthouse Mesa instability, is larger than observed daily (16%) and annual (29%) temperature-driven frequency changes at this site (Moore, 2013), indicating that such a decrease would be evident in monitoring data. However, large environmentally induced frequency fluctuations could mask subtle decreases associated with intermediate failure stages. Temperature-driven frequency responses for unstable rock slopes may also depend on the failure mode (e.g., Bottelin, Jongmans, et al., 2013) or damage state, emphasizing the importance of site-specific evaluations to understand permanent resonance changes in the context of reversible frequency drifts.

In contrast to rock compartments (i.e., slab toppling), field measurements at unstable rock slopes commonly reveal complex resonance behavior that is dependent on the rock mass structure. Model results from our study showing narrow spectral peaks with high amplitude ratios for the flexural toppling case are consistent with field observations at sites with wide-aperture or deep compliant tension cracks (Burjánek et al., 2010, 2018; Häusler et al., 2021; Kleinbrod et al., 2019; Moore et al., 2011). In contrast, instabilities lacking coherent near-vertical fractures (termed depth-controlled by Kleinbrod et al. (2019)) more commonly show limited resonance behavior. These sites include instabilities with sliding kinematics and have seismic responses dominated by horizontally propagating surface waves varying with property changes at depth, in contrast to standing waves characteristic of resonance (Kleinbrod et al., 2019). In the sliding case, frequency changes were detectable due to open cracks created via internal failure; however, the overall resonance response was likely limited by the failure mode. Furthermore, fundamental normal mode resonance of large, deep-seated failures may be weak or difficult to distinguish, and spectral peaks corresponding to sub-volumes in highly fractured areas may dominate the seismic response (Häusler et al., 2021, 2022; Moore, Geimer, Burjánek, et al., 2018). Ultimately, resonance monitoring for damage detection is well-suited for toppling landslides and sliding failures involving tension crack development via internal fracture but may be limited at sites without coherent sub-vertical fractures or for complex deep-seated instabilities. At sites where resonance behavior is not detectable, seismic velocity data from ambient surface-wave dispersion measurements or active seismic surveys may be useful for monitoring landslide failure development (e.g., Bottelin, Jongmans, et al., 2013; Kleinbrod et al., 2017, 2019).

The numerical results described herein can help inform the anticipated resonance behavior at unstable rock sites supporting in situ characterization and monitoring studies. For example, frequency tracking and examination of amplification patterns may be able to inform hypotheses regarding landslide failure mechanisms. Our results demonstrated differences in the 2D amplification patterns along landslide profiles for failures dominated by flexural toppling versus sliding. For instance, resonance frequencies were variably shared across array stations for the flexural toppling and sliding cases, showing more smaller-volume blocks with distinct frequencies in the flexural toppling case and larger blocks with common frequencies in the sliding case. In both cases, the resonance frequency nearest the slope crest (station M1) was shared across several stations during various failure stages; however, neither case exemplified a single resonance frequency consistent across all array stations. Flexural toppling models revealed clear spectral peaks at M1 and a fundamental frequency decrease of 60%. In contrast, sliding models showed a relatively small frequency decrease at M1 (22%) despite similar relative amounts of joint failure. The number of stations sharing a common resonance frequency with M1 decreased during the failure of the flexural toppling case but remained constant during sliding failure (common resonance frequency across stations M1–M5 during stages p2–p6). This observation also indicates that landslides with more complex geometries may not show a single resonance frequency associated with the bulk underlying instability, as typically observed for simple failure geometries such as slab toppling.

For both the flexural toppling and sliding cases, spectral peaks associated with sub-volumes of the main landslide body disappeared, split, decreased, or increased during damage accumulation. This result emphasizes the importance of array measurements since frequency tracking at any given station may not yield straightforward monitoring results. In addition, detailed structural characterization via fracture network mapping and measurements is critical for interpretations of resonance across the landslide. Frequency-dependent polarization analysis and identification of phase relationships between the main landslide body and sub-volumes can also aid in recognition of block evolution during progressive failure (Burjánek et al., 2010, 2012, 2018; Häusler et al., 2021, 2022; Kleinbrod et al., 2019). Comparisons of numerical modeling results with field-based array characterization and monitoring experiments offer promising directions of future research. Such investigations are important to verify numerical results and test the implementation of these techniques in complex field settings. For example, the effects of the 2D approximation inherent to our models should be examined. We anticipate minor differences in the results of the slab toppling case due to the relatively simple geometry, but the flexural toppling and sliding cases are likely more complex in 3D, emphasizing the importance of comparative in situ studies. Ultimately, studies aimed at comparing the results of idealized conceptual modeling with field sites consisting of complex geometries and material conditions are an important avenue for the advancement of in situ ambient vibration measurements for landslide characterization and monitoring.

5. Conclusions

Distinct-element rock slope instability damage modeling demonstrated discernible frequency decreases for progressive slab toppling, flexural toppling, and planar sliding failures. Our results showed that resonance frequencies were most pronounced and easily detectable for slab and flexural toppling geometries. The fundamental frequency of the slab toppling failure decreased according to an analytical power law relationship with the open depth of the main rear discontinuity. In contrast, the resonance frequencies of the flexural toppling and planar sliding failures decreased linearly with the total length of open joints. Changes to higher-order frequencies associated with the development and evolution of landslide sub-volumes could be tracked during subsequent stages of sliding and flexural toppling failures. Although the effects of internal rock mass damage were minimal for the slab toppling case, Voronoi joint failure was a crucial control on spectral evolution of the flexural toppling and sliding cases. Our model results provide new information on anticipated changes in resonance behavior during progressive failure for multiple landslide kinematic modes. The results of this study can be used to inform field investigations of unstable rock slopes by highlighting site dependencies of ambient vibration measurements and aiding in the design of monitoring networks.

Data Availability Statement

The code used to generate UDEC simulations and the resulting time-series outputs are available from The Hive: University of Utah Research Data Repository (Jensen & Moore, 2023).

Acknowledgments

This study was funded by the National Science Foundation grant CMMI-2150896, the Itasca Educational Partnership Research Program, and the David S. and Inga M. Chapman Fund. We are grateful for consultation from Valentin Gischig on modeling steps and UDEC troubleshooting. We additionally thank David DeGagné for additional help with UDEC and Brian Collins for feedback that improved this work. Insightful suggestions that improved this manuscript were also provided by two anonymous reviewers.

References

Alikarami, R., Torabi, A., Kolyukhin, D., & Skurtveit, E. (2013). Geostatistical relationships between mechanical and petrophysical properties of deformed sandstone. *International Journal of Rock Mechanics and Mining Sciences*, *63*, 27–38. https://doi.org/10.1016/j.ijrmms.2013.06.002

Asimaki, D., & Mohammadi, K. (2018). On the complexity of seismic waves trapped in irregular topographies. *Soil Dynamics and Earthquake Engineering*, *114*, 424–437. https://doi.org/10.1016/j.soildyn.2018.07.020

Barton, N. (1976). The shear strength of rock and rock joints. *International Journal of Rock Mechanics and Mining Sciences & Geomechanics Abstracts*, *13*(9), 255–279. https://doi.org/10.1016/0148-9062(76)90003-6

Barton, N., & Choubey, V. (1977). The shear strength of rock joints in theory and practice. *Rock Mechanics*, *10*(1–2), 1–54. https://doi.org/10.1007/BF01261801

Bessette-Kirton, E. K., Moore, J. R., Geimer, P. R., Finnegan, R., Häusler, M., & Dzubay, A. (2022). Structural characterization of a toppling rock slab from array-based ambient vibration measurements and numerical modal analysis. *Journal of Geophysical Research: Earth Surface*, *127*(8), e2022JF006679. https://doi.org/10.1029/2022JF006679

Bottelin, P., Baillet, L., Larose, E., Jongmans, D., Hantz, D., Brenguier, O., et al. (2017). Monitoring rock reinforcement works with ambient vibrations: La Bourne case study (Vercors, France). *Engineering Geology*, *226*, 136–145. https://doi.org/10.1016/j.enggeo.2017.06.002

Bottelin, P., Jongmans, D., Baillet, L., Lebourg, T., Hantz, D., Lévy, C., et al. (2013). Spectral analysis of prone-to-fall rock compartments using ambient vibrations. *Journal of Environmental and Engineering Geophysics*, *18*(4), 205–217. https://doi.org/10.2113/JEEG18.4.205

Bottelin, P., Lévy, C., Baillet, L., Jongmans, D., & Guéguen, P. (2013). Modal and thermal analysis of Les Arches unstable rock column (Vercors massif, French Alps). *Geophysical Journal International*, *194*(2), 849–858. https://doi.org/10.1093/gji/ggt046

Burjánek, J., Gassner-Stamm, G., Poggi, V., Moore, J. R., & Fäh, D. (2010). Ambient vibration analysis of an unstable mountain slope. *Geophysical Journal International*, *180*(2), 820–828. https://doi.org/10.1111/j.1365-246X.2009.04451.x

Burjánek, J., Gischig, V., Moore, J. R., & Fäh, D. (2018). Ambient vibration characterization and monitoring of a rock slope close to collapse. *Geophysical Journal International*, *212*(1), 297–310. https://doi.org/10.1093/gji/ggx424

Burjánek, J., Kleinbrod, U., & Fäh, D. (2019). Modeling the seismic response of unstable rock mass with deep compliant fractures. *Journal of Geophysical Research: Solid Earth*, *124*(12), 13039–13059. https://doi.org/10.1029/2019JB018607

Burjánek, J., Moore, J. R., Yugsi Molina, F. X., & Fäh, D. (2012). Instrumental evidence of normal mode rock slope vibration: Evidence of normal mode rock slope vibration. *Geophysical Journal International*, *188*(2), 559–569. https://doi.org/10.1111/j.1365-246X.2011.05272.x

Chopra, A. K. (2012). *Dynamics of structures*. Pearson Education.

Colombero, C., Baillet, L., Comina, C., Jongmans, D., Larose, E., Valentin, J., & Vinciguerra, S. (2018). Integration of ambient seismic noise monitoring, displacement and meteorological measurements to infer the temperature-controlled long-term evolution of a complex prone-to-fall cliff. *Geophysical Journal International*, *213*(3), 1876–1897. https://doi.org/10.1093/gji/ggy090

Colombero, C., Jongmans, D., Fiolleau, S., Valentin, J., Baillet, L., & Bièvre, G. (2021). Seismic noise parameters as indicators of reversible modifications in slope stability: A review. *Surveys in Geophysics*, *42*(2), 339–375. https://doi.org/10.1007/s10712-021-09632-w

Crosta, G. B., & Agliardi, F. (2003). Failure forecast for large rock slides by surface displacement measurements. *Canadian Geotechnical Journal*, *40*(1), 176–191. https://doi.org/10.1139/t02-085

Cundall, P. A. (1980). UDEC – A generalised distinct element program for modelling jointed rock. *Final Technical Report, European Research Office U. S. Army, Contract DAJA37-79-C-0548*. Retrieved from https://apps.dtic.mil/sti/pdfs/ADA087610.pdf

Cundall, P. A., & Hart, R. D. (1992). Numerical modelling of discontinua. *Engineering Computations*, *9*(2), 101–113. https://doi.org/10.1108/eb023851

Del Gaudio, V., Wasowski, J., & Muscillo, S. (2013). New developments in ambient noise analysis to characterise the seismic response of landslide-prone slopes. *Natural Hazards and Earth System Sciences*, *13*(8), 2075–2087. https://doi.org/10.5194/nhess-13-2075-2013

Dietze, M., Krautblatter, M., Illien, L., & Hovius, N. (2021). Seismic constraints on rock damaging related to a failing mountain peak: The Hochvogel, Allgäu. *Earth Surface Processes and Landforms*, *46*(2), 417–429. https://doi.org/10.1002/esp.5034

Eberhardt, E., Stead, D., & Coggan, J. S. (2004). Numerical analysis of initiation and progressive failure in natural rock slopes—The 1991 Randa rockslide. *International Journal of Rock Mechanics and Mining Sciences*, *41*(1), 69–87. https://doi.org/10.1016/S1365-1609(03)00076-5

Finnegan, R., Moore, J. R., Geimer, P. R., Bessette-Kirton, E. K., & Dzubay, A. (2022). Ground motion amplification at natural rock arches in the Colorado Plateau. *The Seismic Record*, *2*(3), 156–166. https://doi.org/10.1785/0320220017

Fischer, L., Amann, F., Moore, J. R., & Huggel, C. (2010). Assessment of periglacial slope stability for the 1988 Tschierva rock avalanche (Piz Morteratsch, Switzerland). *Engineering Geology*, *116*(1–2), 32–43. https://doi.org/10.1016/j.enggeo.2010.07.005

Frayssines, M., & Hantz, D. (2009). Modelling and back-analysing failures in steep limestone cliffs. *International Journal of Rock Mechanics and Mining Sciences*, *46*(7), 1115–1123. https://doi.org/10.1016/j.ijrmms.2009.06.003

Fukuzono, T. (1985). A method to predict the time of slope failure caused by rainfall using the inverse number of velocity of surface displacement. *Journal of Japan Landslide Society*, *22*(2), 8–13. https://doi.org/10.3313/jls1964.22.2_8

Galea, P., D'Amico, S., & Farrugia, D. (2014). Dynamic characteristics of an active coastal spreading area using ambient noise measurements—Anchor Bay, Malta. *Geophysical Journal International*, *199*(2), 1166–1175. https://doi.org/10.1093/gji/ggu318

Geimer, P. R., Finnegan, R., & Moore, J. R. (2022). Meteorological controls on reversible resonance changes in natural rock arches. *Journal of Geophysical Research: Earth Surface*, *127*(10), e2022JF006734. https://doi.org/10.1029/2022JF006734

Gischig, V. S., Eberhardt, E., Moore, J. R., & Hungr, O. (2015). On the seismic response of deep-seated rock slope instabilities—Insights from numerical modeling. *Engineering Geology*, *193*, 1–18. https://doi.org/10.1016/j.enggeo.2015.04.003

Gischig, V. S., Moore, J. R., Evans, K. F., Amann, F., & Loew, S. (2011a). Thermomechanical forcing of deep rock slope deformation: 1. Conceptual study of a simplified slope. *Journal of Geophysical Research*, *116*(F4), F04010. https://doi.org/10.1029/2011JF002006

Gischig, V. S., Moore, J. R., Evans, K. F., Amann, F., & Loew, S. (2011b). Thermomechanical forcing of deep rock slope deformation: 2. The Randa rock slope instability. *Journal of Geophysical Research*, *116*(F4), F04011. https://doi.org/10.1029/2011JF002007

Gischig, V. S., Preisig, G., & Eberhardt, E. (2016). Numerical investigation of seismically induced rock mass fatigue as a mechanism contributing to the progressive failure of deep-seated landslides. *Rock Mechanics and Rock Engineering*, *49*(6), 2457–2478. https://doi.org/10.1007/s00603-015-0821-z

Glueer, F., Häusler, M., Gischig, V., & Fäh, D. (2021). Coseismic stability assessment of a damaged underground ammunition storage chamber through ambient vibration recordings and numerical modelling. *Frontiers in Earth Science*, *9*, 773155. https://doi.org/10.3389/feart.2021.773155

Goodman, R. E. (1989). *Introduction to rock mechanics* (2nd ed.). John Wiley & Sons.

Goodman, R. E., & Bray, J. W. (1976). Toppling of rock slopes. In *Proceedings of the Specialty Conference on Rock Engineering for Foundations and Slopes*. American Society of Civil Engineers.

Got, J.-L., Mourot, P., & Grangeon, J. (2010). Pre-failure behaviour of an unstable limestone cliff from displacement and seismic data. *Natural Hazards and Earth System Sciences*, *10*(4), 819–829. https://doi.org/10.5194/nhess-10-819-2010

Grämiger, L. M., Moore, J. R., Gischig, V. S., Ivy-Ochs, S., & Loew, S. (2017). Beyond debuttressing: Mechanics of paraglacial rock slope damage during repeat glacial cycles. *Journal of Geophysical Research: Earth Surface*, *122*(4), 1004–1036. https://doi.org/10.1002/2016JF003967

Guillemot, A., Baillet, L., Larose, E., & Bottelin, P. (2022). Changes in resonance frequency of rock columns due to thermoelastic effects on a daily scale: Observations, modelling and insights to improve monitoring systems. *Geophysical Journal International*, *231*(2), 894–906. https://doi.org/10.1093/gji/ggac216

Harris, C. R., Millman, K. J., van der Walt, S. J., Gommers, R., Virtanen, P., Cournapeau, D., et al. (2020). Array programming with NumPy. *Nature*, *585*(7825), 357–362. https://doi.org/10.1038/s41586-020-2649-2

Häusler, M., Gischig, V., Thöny, R., Glueer, F., & Donat, F. (2022). Monitoring the changing seismic site response of a fast-moving rockslide (Brienz/Brinzauls, Switzerland). *Geophysical Journal International*, *229*(1), 299–310. https://doi.org/10.1093/gji/ggab473

Häusler, M., Michel, C., Burjánek, J., & Fäh, D. (2019). Fracture network imaging on rock slope instabilities using resonance mode analysis. *Geophysical Research Letters*, *46*(12), 6497–6506. https://doi.org/10.1029/2019GL083201

Häusler, M., Michel, C., Burjánek, J., & Fäh, D. (2021). Monitoring the Preonzo rock slope instability using resonance mode analysis. *Journal of Geophysical Research: Earth Surface*, *126*(4), e2020JF005709. https://doi.org/10.1029/2020JF005709

Higgins, J. D., & Andrew, R. D. (2012). Rockfall types and causes. In A. K. Turner & R. L. Schuster (Eds.), *Rockfall Characterization and Control*. Transportation Research Board of the National Academies.

Iannucci, R., Martino, S., Paciello, A., D'Amico, S., & Galea, P. (2018). Engineering geological zonation of a complex landslide system through seismic ambient noise measurements at the Selmun Promontory (Malta). *Geophysical Journal International*, *213*(2), 1146–1161. https://doi.org/10.1093/gji/ggy025

Intrieri, E., Carlà, T., & Gigli, G. (2019). Forecasting the time of failure of landslides at slope-scale: A literature review. *Earth-Science Reviews*, *193*, 333–349. https://doi.org/10.1016/j.earscirev.2019.03.019

Itasca Consulting Group. (2019). Universal distinct element code user's guide, version 7.0.

Jennings, J. E. (1970). A mathematical theory for the calculation of the stability of open cast mines. In *Symposium on the Theoretical Background to the Planning of Open Pit Mines*.

Jensen, E. K., & Moore, J. R. (2023). Ambient vibration simulations of damaged rock slopes using distinct-element modeling [Dataset]. The Hive: University of Utah Research Data Repository. https://doi.org/10.7278/S50d-j662-kdt9

Kleinbrod, U., Burjánek, J., & Fäh, D. (2019). Ambient vibration classification of unstable rock slopes: A systematic approach. *Engineering Geology*, *249*, 198–217. https://doi.org/10.1016/j.enggeo.2018.12.012

Kleinbrod, U., Burjánek, J., Hugentobler, M., Amann, F., & Fäh, D. (2017). A comparative study on seismic response of two unstable rock slopes within same tectonic setting but different activity level. *Geophysical Journal International*, *211*(3), 1428–1448. https://doi.org/10.1093/gji/ggx376

Kulhawy, F. H. (1975). Stress deformation properties of rock and rock discontinuities. *Engineering Geology*, *9*(4), 327–350. https://doi.org/10.1016/0013-7952(75)90014-9

Lévy, C., Baillet, L., Jongmans, D., Mourot, P., & Hantz, D. (2010). Dynamic response of the Chamousset rock column (Western Alps, France). *Journal of Geophysical Research*, *115*(F4), F04043. https://doi.org/10.1029/2009JF001606

Lorig, L. J., Watson, A. D., Martin, C. D., & Moore, D. P. (2009). Rockslide run-out prediction from distinct element analysis. *Geomechanics and Geoengineering*, *4*(1), 17–25. https://doi.org/10.1080/17486020902767321

Mamot, P., Weber, S., Eppinger, S., & Krautblatter, M. (2021). A temperature-dependent mechanical model to assess the stability of degrading permafrost rock slopes. *Earth Surface Dynamics*, *9*(5), 1125–1151. https://doi.org/10.5194/esurf-9-1125-2021

Moore, J. R. (2013). Structural health monitoring of rock arches and towers [Dataset]. International Federation of Digital Seismograph Networks. https://doi.org/10.7914/SN/5P_2013

Moore, J. R., Geimer, P. R., Burjánek, J., Gibbons, D., & Malone, S. D. (2018). Seismic monitoring of the Rattlesnake ridge rockslide, Union Gap, Washington. In *2018 Seismology of the Americas Meeting* (Vol. 89, p. 250). Seismological Research Letters.

Moore, J. R., Geimer, P. R., Finnegan, R., & Thorne, M. S. (2018). Use of seismic resonance measurements to Determine the elastic modulus of freestanding rock masses. *Rock Mechanics and Rock Engineering*, *51*(12), 3937–3944. https://doi.org/10.1007/s00603-018-1554-6

Moore, J. R., Gischig, V., Burjanek, J., Amann, F., & Hunziker, M. (2012). Earthquake-triggered rock slope failures: Damage and site effects. In *Proceedings of the 11th International & 2nd North American Symposium of Landslides, Banff, BC*. Retrieved from https://geohazards.earth.utah.edu/images/Moore_et al._ISL12_v2.pdf

Moore, J. R., Gischig, V., Burjanek, J., Loew, S., & Fah, D. (2011). Site effects in unstable rock slopes: Dynamic behavior of the Randa instability (Switzerland). *Bulletin of the Seismological Society of America*, *101*(6), 3110–3116. https://doi.org/10.1785/0120110127

Mufundirwa, A., Fujii, Y., & Kodama, J. (2010). A new practical method for prediction of geomechanical failure-time. *International Journal of Rock Mechanics and Mining Sciences*, *47*(7), 1079–1090. https://doi.org/10.1016/j.ijrmms.2010.07.001

Petley, D. N. (2004). The evolution of slope failures: Mechanisms of rupture propagation. *Natural Hazards and Earth System Sciences*, *4*(1), 147–152. https://doi.org/10.5194/nhess-4-147-2004

Rose, N. D., & Hungr, O. (2007). Forecasting potential rock slope failure in open pit mines using the inverse-velocity method. *International Journal of Rock Mechanics and Mining Sciences*, *44*(2), 308–320. https://doi.org/10.1016/j.ijrmms.2006.07.014

Skurtveit, E., Torabi, A., Sundal, A., & Braathen, A. (2021). The role of mechanical stratigraphy on CO_2 migration along faults – Examples from Entrada Sandstone, Humbug Flats, Utah, USA. *International Journal of Greenhouse Gas Control*, *109*, 103376. https://doi.org/10.1016/j.ijggc.2021.103376

Taruselli, M., Arosio, D., Longoni, L., Papini, M., & Zanzi, L. (2020). Seismic noise monitoring of a small rock block collapse test. *Geophysical Journal International*, *224*(1), 207–215. https://doi.org/10.1093/gji/ggaa447

Valentin, J., Capron, A., Jongmans, D., Baillet, L., Bottelin, P., Donze, F., et al. (2017). The dynamic response of prone-to-fall columns to ambient vibrations: Comparison between measurements and numerical modelling. *Geophysical Journal International*, *208*(2), 1058–1076. https://doi.org/10.1093/gji/ggw440

Wang, G. L., Wu, F. Q., & Ye, W. J. (2013). Stability analysis for toppling failure of unstable rock in Three Gorges Reservoir Area, China. In X.-T. Feng, J. A. Hudson, & F. Tan (Eds.), *Rock Characterisation, Modelling and Engineering Design Methods*. CRC Press. https://doi.org/10.1201/b14917

Weber, S., Fäh, D., Beutel, J., Faillettaz, J., Gruber, S., & Vieli, A. (2018). Ambient seismic vibrations in steep bedrock permafrost used to infer variations of ice-fill in fractures. *Earth and Planetary Science Letters*, *501*, 119–127. https://doi.org/10.1016/j.epsl.2018.08.042

Wyllie, D. C. (1980). Toppling rock slope failures—Examples of analysis and stabilization. *Rock Mechanics*, *13*(2), 89–98. https://doi.org/10.1007/bf01238952

Wyllie, D. C., & Mah, C. W. (2005). *Rock slope engineering, civil and mining* (4th ed.). Taylor & Francis Group.

Wyllie, D. C., & Norrish, N. I. (1996). Rock strength properties and their measurement. In A. K. Turner & R. L. Schuster (Eds.), *Landslides investigation and mitigation* (pp. 372–390). National Academies Press.